Journal of Materials Chemistry A

Additive engineered SnO_2-based electron transport layer for the robust and high-efficiency large-scale perovskite solar cell

Journal:	*Journal of Materials Chemistry A*
Manuscript ID	TA-ART-08-2024-005866.R1
Article Type:	Paper
Date Submitted by the Author:	30-Oct-2024

Complete List of Authors:	Kim, Byeong Jo; Uppsala Universitet, Department of Chemistry-Ångström Laboratory Seo , Gabseok ; UniTest Incorporation, PSC R&D Department Park, Sua; Pusan National University Lee, Donghyeon; Pusan National University, School of Mechanical Engineering Luo, Yanqi; Argonne National Laboratory Advanced Photon Source Wieghold, Sarah; Argonne National Laboratory, APS, CNM Kim, Min-cheol; Pusan National University, School of Mechanical Engineering Boschloo, Gerrit; Uppsala Universitet, Department of Chemistry-Ångström Laboratory

ARTICLE

Additive engineered SnO_2-based electron transport layer for the robust and high-efficiency large-scale perovskite solar cell†

Received 00th January 20xx,
Accepted 00th January 20xx

DOI: 10.1039/x0xx00000x

Byeong Jo Kim[a§], Gabseok Seo[b§], Sua Park[c], Donghyeon Lee[c], Yanqi Luo[d], Sarah Wieghold[d], Min-cheol Kim[c]*, Gerrit Boschloo[a]*

The efficient production of uniform, high-quality transport layers beneath the light-absorbing layer is crucial for the performance and scalability of perovskite solar cells (PSCs). This study investigates the incorporation of potassium fluoride (KF) into tin dioxide (SnO2) nanoparticle solutions to enhance the properties of the electron transport layer (ETL) in PSCs. By introducing KF, we observed a significant reduction in SnO2 particle size and improved zeta potential, resulting in a more uniform ETL. Experimental analysis demonstrated that optimal KF concentrations in SnO2 nanoparticles improved coverage and uniformity on substrates, as confirmed by surface SEM and AFM measurement. Such improvement in ETL morphology reduced charge recombination and increased charge carrier mobility of PSCs. Specifically, PSCs with 0.02 M of KF addition showed increased power conversion efficiencies (PCE), up to 24.3%. Furthermore, large-area PSC modules with a 25 cm2 aperture area exhibited an average PCE enhancement up to 18.0% due to superior ETL uniformity. Additionally, KF addition also aided the stability enhancement, maintaining 90% of their initial efficiency after 250 hours under 60 ± 5% relative humidity. Our findings underscore the importance of ETL uniformity and provide insights into the role of KF doping in advancing PSC performance, paving the way for more efficient and scalable solar energy solutions.

Introduction

Due to its abundance and environmental sustainability, solar energy has gained substantial attention as a viable alternative to conventional fossil fuel-based energy sources.[1] The perovskite solar cell (PSC), based on organic–inorganic halide perovskite materials, has emerged as one of the most promising photovoltaic technologies, owing to its remarkable efficiency improvements, with low fabrication cost, high flexibility, and great optoelectronic properties.[2-4] The power conversion efficiency (PCE) of the PSC has rapidly increased from a few percent to over 26 % within 15 years, and currently exhibits identical performance to the traditional silicon-based solar cell.[5] The high-efficiency PSC predominantly utilizes a structure known as n–i–p, which is characterized by distinct layers: the electron transport layer (ETL), the perovskite absorber layer, and the hole transport layer (HTL).[6] The ETL is deposited before the perovskite layer, and thus has a significant influence on the performance of the perovskite absorber layer. It plays a crucial role in facilitating efficient charge extraction and transport, and assists in rapid electron transfer from the perovskite layer to the electrode, reducing recombination losses, and enhancing the overall device performance.[7-9] It significantly impacts the performance of the PSC, while also playing a crucial role in ensuring its long-term stability.[10,11] For the appropriate selection of an ETL in the PSC, various optical, electrical, and chemical properties must be considered.[12] Suitable energy level of the selected ETL, high electrical conductivity, and elevated transparency can enhance the performance of the PSC. From the perspective of stability and process robustness, the ETL should be chemically stable, non-reactive with the perovskite precursor, and exhibit excellent morphology and surface quality. High-efficiency PSCs primarily uses metal oxides or fullerene derivatives as ETL.[13]

Among ETLs, Tin dioxide (SnO_2) has gained considerable attention as a promising material in the PSC, due to its excellent electrical conductivity, transparency, and ease of fabrication.[14,15] Various SnO_2 deposition methods are used, including techniques that utilize SnO_2 nanoparticles,[16] chemical bath deposition,[17] and vapor deposition processes, such as thermal evaporation or atomic layer deposition (ALD).[18,19] Among these, the method of depositing SnO_2 via a solution process using SnO_2 nanoparticle colloidal dispersion has the advantage of environment-friendliness, cost-effectiveness, and simple fabrication process, due to the use of deionized water as the solvent. This feature provides high accessibility and compatibility, making it suitable for commercialization. Exploiting these advantages, the high-efficiency colloidal SnO_2-based PSC has been reported in the literature for quite some time, albeit mainly focused on the small-area solar cell.[20-22] However, to progress from small-area solar cell to the large-

[a] Department of Chemistry – Angstrom Laboratory, Physical Chemistry, Box 523, Uppsala University SE-751 20 Uppsala, Sweden.
[b] PSC R&D Dept, UniTest Inc. Pyeongtaek 17791, Republic of Korea.
[c] School of Mechanical Engineering, Pusan National University, Busan 46241, Republic of Korea.
[d] Advanced Photon Source, Argonne National Laboratory, Lemont, Illinois 60439, United States.
§These authors contribute equally to this work

†Electronic Supplementary Information (ESI) available: See DOI:

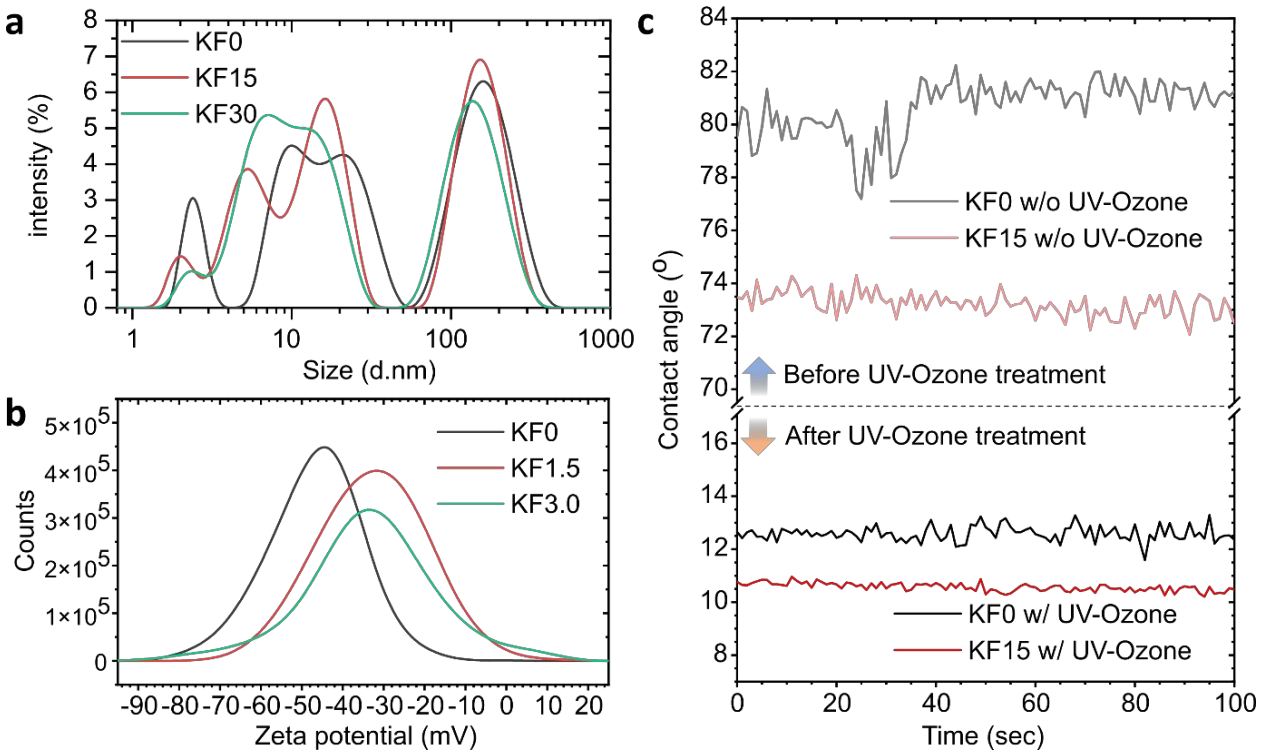

Figure 1. The (a) DLS size distribution, and (b) zeta potential values for the KF0, KF15, and KF30:SnO_2. (c) The contact angle value of the KF0 and KF15:SnO_2 on the FTO/glass substrate before (above) and after (below) UV-ozone treatment.

area and module-scale device, it is crucial to achieve a pinhole-free and uniform SnO_2 ETL, which is currently only achieved by chemical bath deposition.[17] Unfortunately, when colloidal nanoparticle-based SnO_2 coatings have been applied to large-area substrates, uneven deposition has been reported as a problematic issue.[23,24] These studies have highlighted the need for special additive treatments to achieve uniform deposition. Nevertheless, existing research has primarily focused on empirical interpretations based on the use of specific additives, lacking in-depth analysis regarding the changes in colloidal particle motion and the resulting optoelectronic effects that enable large-area coating. Furthermore, the overall efficiency of such large-area coatings remains suboptimal.

To overcome these limitations and improve the performance of the SnO_2-based ETL, various strategies have been explored, including the incorporation of dopants to modify the electronic properties and surface morphology of SnO_2 nanoparticles. In this study, we focus on the incorporation of potassium fluoride (KF) into SnO_2 nanoparticle solutions as a dopant to enhance the performance of the perovskite solar cell. KF has been widely utilized as a dopant in different semiconductor materials, due to its ability to modify their electronic properties and surface characteristics.[25,26] The introduction of KF into SnO_2 nanoparticles can potentially reduce the number of surface defects, enhance the charge carrier mobility, and improve the overall charge extraction efficiency.

Our results show that the addition of KF can improve the performance of the device by improving the uniformity of the SnO_2 ETL, which is attributed to the change in particle size distribution and zeta potential of the SnO_2 colloidal solution. Additionally, the improved uniformity of the SnO_2 ETL leads to a reduction in charge recombination, and an increase in device efficiency. Overall, our study provides insights into the importance of the uniformity of the SnO_2 ETL, and the role of KF in achieving the high-performance large-area PSC. In this study, we investigate the impact of KF on the stabilized colloidal solution of SnO_2 nanoparticles, and its effect on the performance of the PSC. The study analyzes the interaction of the SnO_2 particles with K^+ and F^- ions, and evaluates the changes in particle size distribution, pH value, and zeta potential. PSCs based on SnO_2 with 0.02 M of KF addition exhibited outstanding performance up to 24.3% of PCE without hysteresis behavior, which is greatly enhanced from the reference PSCs without additives with 20.8% of PCE. Moreover, with the uniform deposition of KF added SnO_2 nanoparticles, large area PSC modules with 25 cm^2 aperture area exhibited up to 18.0% of PCE with neglectable hysteresis. With multiple comprehensive investigation of the KF-doped SnO_2-based ETL including dynamic light scattering (DLS), photoluminescence and X-ray based characterization, we aim to shed light on the influence of KF doping on the optoelectronic properties and performance of the PSC.

Results and Discussion

To investigate the impact of the additive, KF, on the colloidal SnO_2 solution, we began by analyzing the commercially available colloidal solution in detail. Stabilization or aggregation

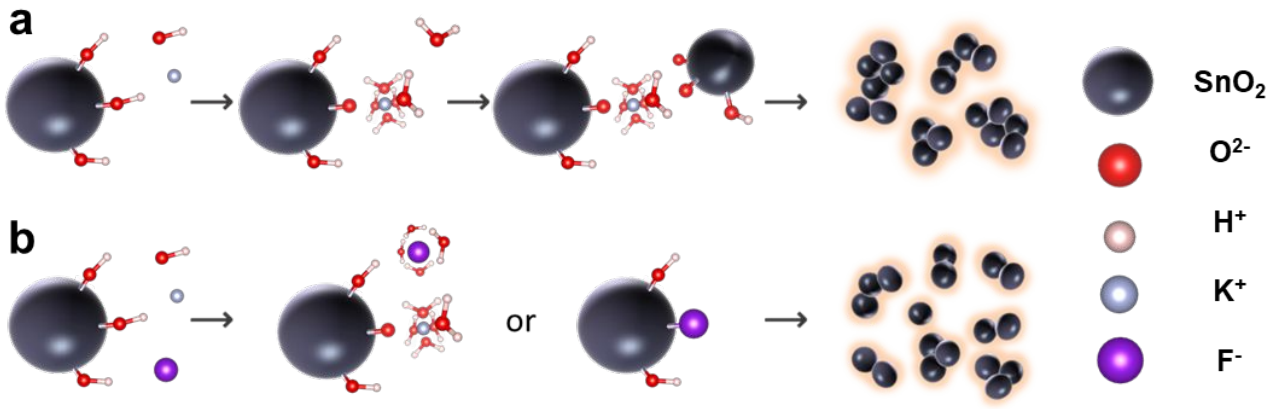

Figure 2. Schematic of the interaction of aqueous SnO_2 colloidal system with (a) K^+ ions, or (b) K^+ and F^- ions.

of nanoparticles in a colloidal solution is influenced by the pH, the ionic strength and by specific adsorption of ions. The addition of KF may affect all these parameters, which could significantly alter the stability or uniformity of the colloidal solution.[27,28] However, at the same time, the addition of KF may lead to the introduction of favorable or unwanted impurities. As a result, when applying an ETL created based on the modified colloidal solution to the PSC, the performance of the solar cell may improve or decrease. Therefore, the first step was to conduct tests to identify an appropriate amount of KF additive that would be favorable to the performance of the PSC. For this purpose, we fabricated devices using various concentrations of KF added to the SnO_2 layer. We prepared SnO_2 dispersion solutions with the addition of (1.5, 3.0, 4.5, and 6.0) mg of KF to 1 mL of high-purity deionized H_2O, which were named as KF15, KF30, KF45, and KF60, respectively. The reference SnO_2, which did not contain any added KF, was designated as KF0. SnO_2 films and PSC devices with specific KF are described as KF:SnO_2 and KF:PSC, respectively. As depicted in Figure S1, the photovoltaic performance of the KF15:PSC and KF30:PSC was superior to that of the KF0:PSC. Plus, adding more than 4.5 mg of KF was clearly detrimental to the performance of PSCs, implying that the appropriate amount of additional KF is 1.5 mg. (This corresponds to a concentration of 0.02 M.)

We further examined the pH value and particle size distribution of the KF0, KF15, and KF30:SnO_2, to better understand the effects of the KF. The KF0:SnO_2 had a rather basic pH value of 11.35, whereas the KF15:SnO_2 and KF30:SnO_2 exhibited slightly lower pH values (11.18 and 11.14), respectively. We used dynamic light scattering (DLS) analysis to determine the mean particle size of the KF0, KF15, and KF30:SnO_2, which were found to be (19.79, 15.65, and 14.4) nm, respectively (see Figure 1a). Importantly, we observed a particle distribution of 100 nm or more, which indicated the presence of agglomerated nanoparticles.[29] The primary SnO_2 nanocrystal size in the colloidal solution is reported to be 3.3 nm.[30] Clearly, most nanoparticles are present as aggregates in the suspension. A reduction of the mean aggregate size will be favorable in forming a uniform film as an ETL, and it corresponded with the trend in PSC performance variation.

These minor changes in pH and particle size distribution can affect the zeta-potential value of the particle surface, which is the fundamental parameter known to affect the stability of colloidal dispersion and wettability of the substrate surface.[31,32] As shown in Figure 1b, the zeta potential difference was approximately 13 mV, depending on the presence or absence of KF. Table S1 summarizes the analyzed data for comparison. Such changes in the zeta potential tend to worsen the stability of the dispersion. However, it was confirmed that both with and without the addition of KF, they can be within the range of highly stable dispersion stability, since all the absolute values of zeta potential were of > 30 mV.[33] On the other hand, this change in zeta potential can result in variations in the wettability of the SnO_2 colloidal solution on the FTO substrate. We measured the contact angle of the KF0 and KF15:SnO_2 dispersions on the FTO surface with and without UV ozone treatment, as shown in Figure 1c. The KF15:SnO_2 exhibited a lower contact angle than the KF0:SnO_2 in both cases, indicating a better wetting of the substrate, leading to smoother and more conformal coating of SnO_2 nanoparticles. The contact angle value and droplet image between the KF:SnO_2 and the FTO/glass before and after UV-ozone treatment can be found in Table S2 and Figure S2, respectively.

Understanding the general colloidal system can help explain the change of particle size distribution and consequence variations in pH and zeta potential. In an aqueous solution of colloidal metal oxide, a large number of primary particles can be easily aggregated or agglomerated through hydrogen bonding or van der Waals forces.[34] For example, as illustrated in Figure S3, hydrated SnO_2 particles attract each other via hydrogen bonding, which can sometimes be weakened by free H_2O molecules. However, by the addition of KF, when K^+ ions are present in an aqueous SnO_2 colloidal solution, the steric effect caused by K^+ surrounded by H_2O, as depicted in Figure 2a, can aid in the formation of agglomerates, which is not favorable for uniform distribution.[35] In contrast, when F^- ions are added, F^- ion binds directly to SnO_2 or is surrounded by H_2O molecules, as shown in Figure 2b, which may inhibit the interaction between particles, reducing the agglomeration of the nanoparticles. Based on the proposed mechanism, it can be predicted that the

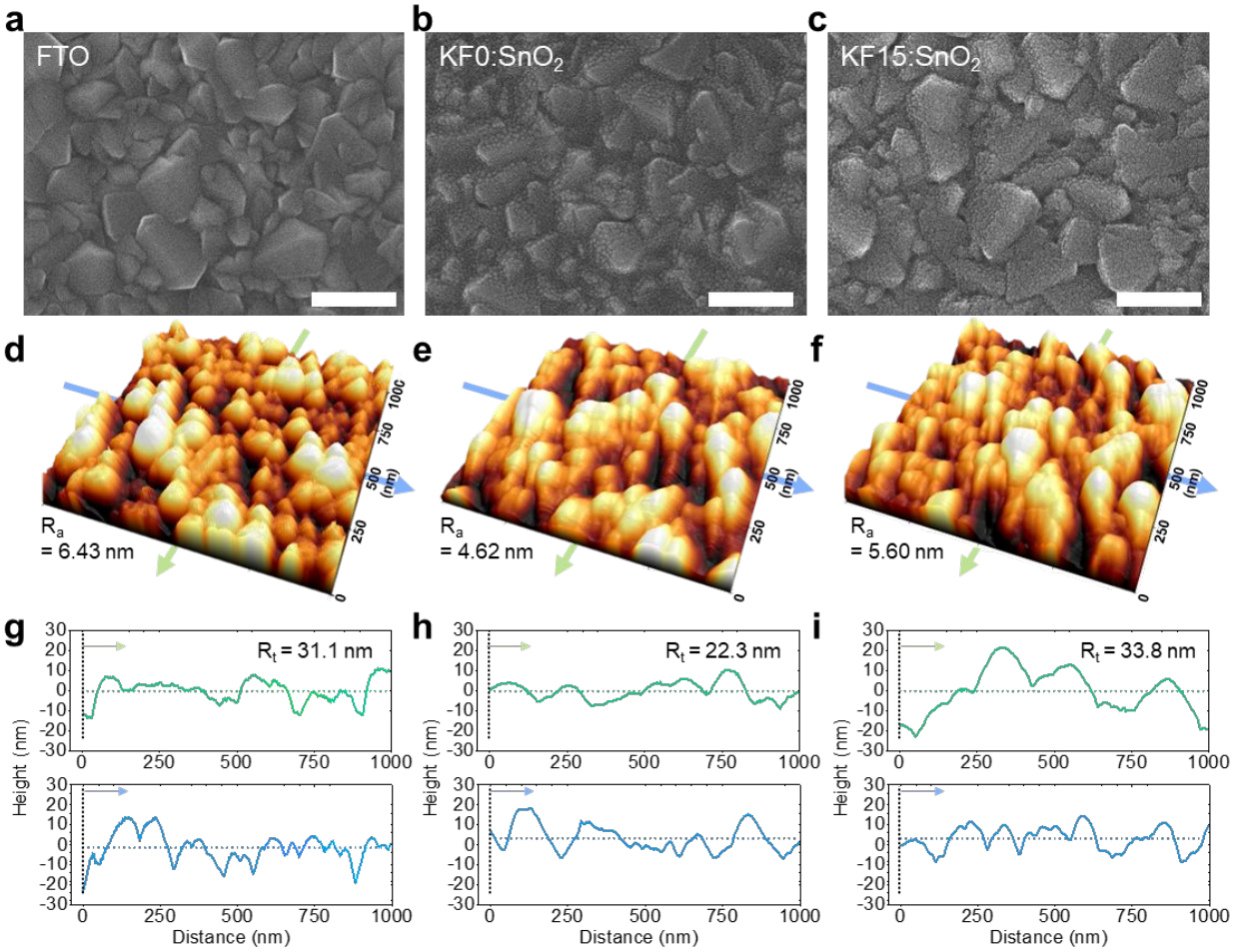

Figure 3. (a)–(c) Plane SEM images, (d)–(f) 3D view of AFM topography and arithmetic mean roughness (R_a), and (f)–(i) AFM line profile (solid line) and mean line (dotted line) corresponding to the green/blue arrows in AFM topography of the (a), (d), and (g) bare FTO, (b), (e), and (h) KF0:SnO_2/FTO, and (c), (f), and (i) KF15:SnO_2/FTO, respectively. Scale bar in the SEM images indicates 500 nm.

change in the mean particle size of the colloidal dispersion obtained by adding KF is mainly due to the effect of F^- ions. Thus, it was confirmed that the addition of KF to the SnO_2 nanoparticle dispersion solution, through the role of F^- ions, does not significantly affect the dispersion stability, yet ensures the wettability of the FTO substrate. Such changes are expected to lead to a uniform coating in fabrication process.

The deposition of spin-coated SnO_2 colloidal films on randomly textured FTO surfaces can result in incomplete and non-uniform coverage, which may induce critical defect sites during the charge transportation process. The formation of self-assembled monolayers of colloidal particles is dependent on proper attractive interaction between the particles and the substrate, whereas the lack of such attractive interaction leads to non-uniform patterns during solvent drying.[36,37] To evaluate the effect of changed zeta potential by adding the KF, KF0 and KF15:SnO_2 solutions were dropped and held for 1 min on the FTO surface, before spin-coating. Figures 3a–c show SEM images of the bare FTO, KF0, and KF15:SnO_2 coated FTO surfaces, respectively. Figure 3b shows that the KF0:SnO_2 coating appears to cover the FTO surface well, but some of the highest points are still exposed, or deep valleys located in the centrifugal force direction remain unfilled. Interestingly, the KF15:SnO_2 coated sample in Figure 3c shows FTO-like morphology and evenly coated tiny nanoparticles along the surface.

Atomic force microscopy (AFM) surface profiling data confirms the SEM imagery. Figures 3d–f and g–i present the 3D AFM topography images and surface line profiling data, respectively. The FTO surface has an arithmetic mean roughness (R_a) of 6.43 nm and maximum peak-to-valley height (R_t) of 31.1 nm in Figures 3d and g. The AFM data of the KF0:SnO_2 coated FTO in Figures 3e and h indicate that the surface profiling below the mean line becomes generally flat, resulting 4.62 nm of R_a and 22.3 nm of R_t. This implies the non-uniform deposition of KF0:SnO_2 filled the valley of rough FTO surface. The roughness above the mean line still showed large fluctuations since the filling mechanism of colloidal particles only affects the valley of the rough surface. The surface profiling data of the KF15:SnO_2 coated FTO in Figures 3f and i show relatively similar R_t (33.8 nm) and R_a values (5.60 nm) to the bare FTO surface, which could be observed when the colloidal particles were uniformly deposited on the surface. In conclusion, the addition of small amounts of K+ and F^- ions to the SnO_2 colloidal solution system

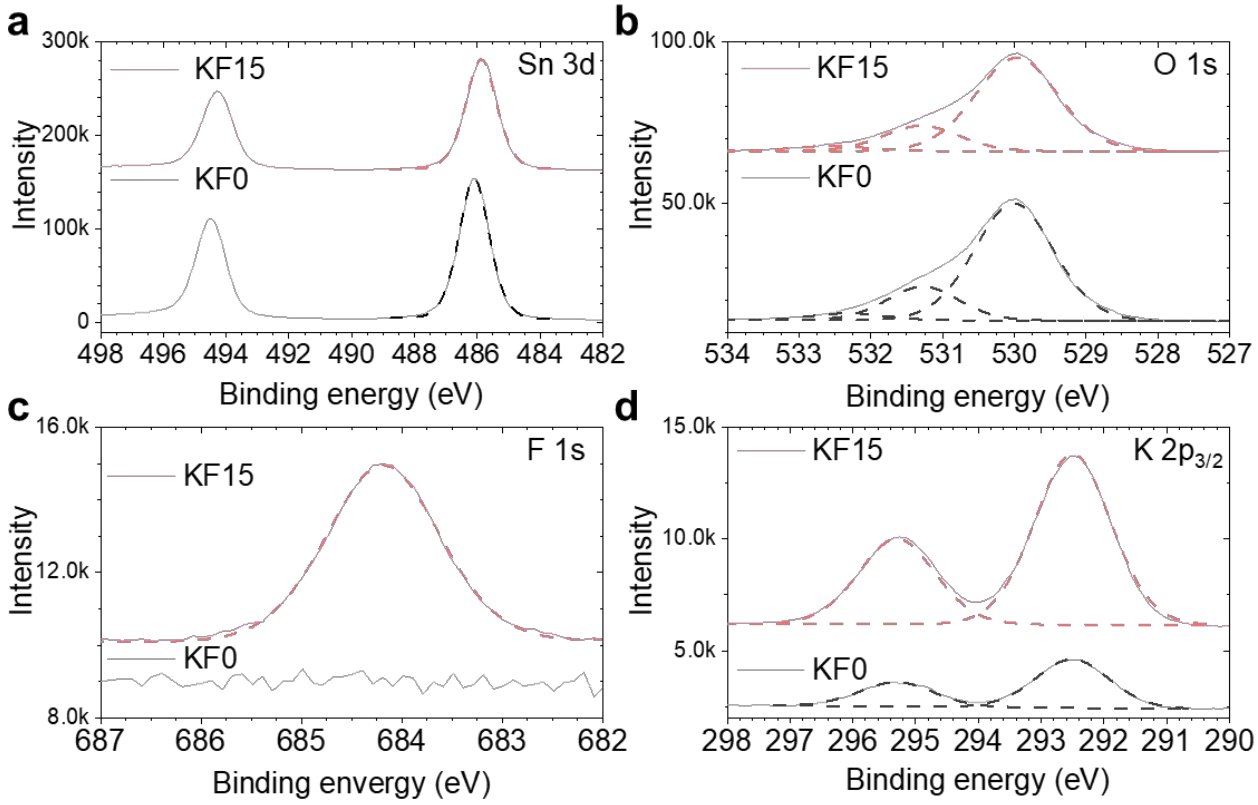

Figure 4. The XPS measurement data of the KF0:SnO2 and KF15:SnO2 samples. The (a) Sn 3d, (b) O 1s, (c) F 1s, and (d) K $2p_{3/2}$ spectra of both samples. Dashed line indicates the de-convoluted curve with Gaussian/Lorentzian (0.3) function.

affects the formation of SnO_2 thin films on rough FTO substrates. The addition of KF to SnO_2 results in conformal coating and excellent coverage, which will function superbly as a hole blocking layer. Figure S4 demonstrates this through the cyclic voltammetry measurements.[38]

Subsequently, we investigated the impact of KF on the properties of the SnO_2 layer, perovskite thin films, and photovoltaic device produced on the KF15:SnO_2 layer. Using X-ray photoelectron spectroscopy (XPS), we assessed whether K+ and F^- were incorporated into the SnO_2 layer; and if so, in what form they exist. We calibrated all XPS spectra using the C 1s peak at 284.5 eV, and present the full range of XPS data and de-convoluted XPS parameters in Figure S5 and Tables S3 and S4. As shown in Figure 4a, the binding energies of the Sn $3d_{5/2}$ for the KF0:SnO_2 and KF15:SnO_2 were (486.1 and 485.87) eV, respectively, which is typical for the oxidation state of Sn^{4+} in SnO_2.[39,40] The downshift of the Sn $3d_{5/2}$ peak occurred if an electronegative anion (such as F^-) surrounded the Sn component. The O 1s peaks were de-convoluted into three components: $O_{lattice}$ (corresponding to lattice oxygen in SnO_2), O_{vac} (corresponding to oxygen in the vicinity of an oxygen vacancy), and −OH groups (Figure 4b).[41,42] We assumed that the −OH group (~532.3 eV) originated from the experimental environment, and thus focused on O_{vac} (~531.2 eV) and $O_{lattice}$ (~529.9 eV). The ratio of $O_{vac}/O_{lattice}$ was slightly higher in the KF0:SnO_2 (26.0 %) than in the KF15:SnO_2 (24.9%), assuming that the surface O_{vac} was passivated by F^- ions. The F 1s peak was detected only in the KF15:SnO_2 at 684.19 eV, and the binding energy of F 1s in the range (484 to 485.5) eV was identified in the form of a metal fluoride state (Figure 4c).[43] Although we cannot conclude that this is purely F^- bonded to the surface Sn, we can strongly assert the existence of Sn–F bonding (as described in Figure 2b), due to the previously described peak shift of Sn 3d. In Figure 4d, the K 2p3/2 peak intensity was also observed in KF0:SnO_2, where KF additives are not included. This is due to the use of a potassium derivative surfactant in the purchased SnO_2 nanoparticle to stabilize the colloidal dispersion. [44] However, the peak intensity of the KF15:SnO_2 was about three times stronger than that of the KF0:SnO_2. Increased K^+ ion more easily formed an alkali–oxygen–metal state, which reduced the surface defect.[45] Furthermore, the chemical binding of K−O−Sn can be supported by the KF15:SnO_2 having a lower binding energy of K $2p_{3/2}$ than the KF0:SnO_2, because during the formation of the K−O−Sn state, the lone 4 s1 electrons are transferred from K^+ to SnO_2.

Although KF has a favorable impact on the chemical state of the SnO_2 layer, this effect may be lost or altered during the perovskite deposition process. Since XPS analysis cannot analyze the underlying layers after perovskite deposition due to its limited penetration power, we employed hard X-ray fluorescence (XRF) mapping to determine whether the K element remains after device fabrication. Figures S6a and b show the XRF mapping data of the full devices for KF0:PSC and KF15:PSC, respectively. The histogram of the K intensity of these two devices is shown in Figure S6c. Since no KF was intentionally added in KF0:PSC device, the detected potassium signal likely

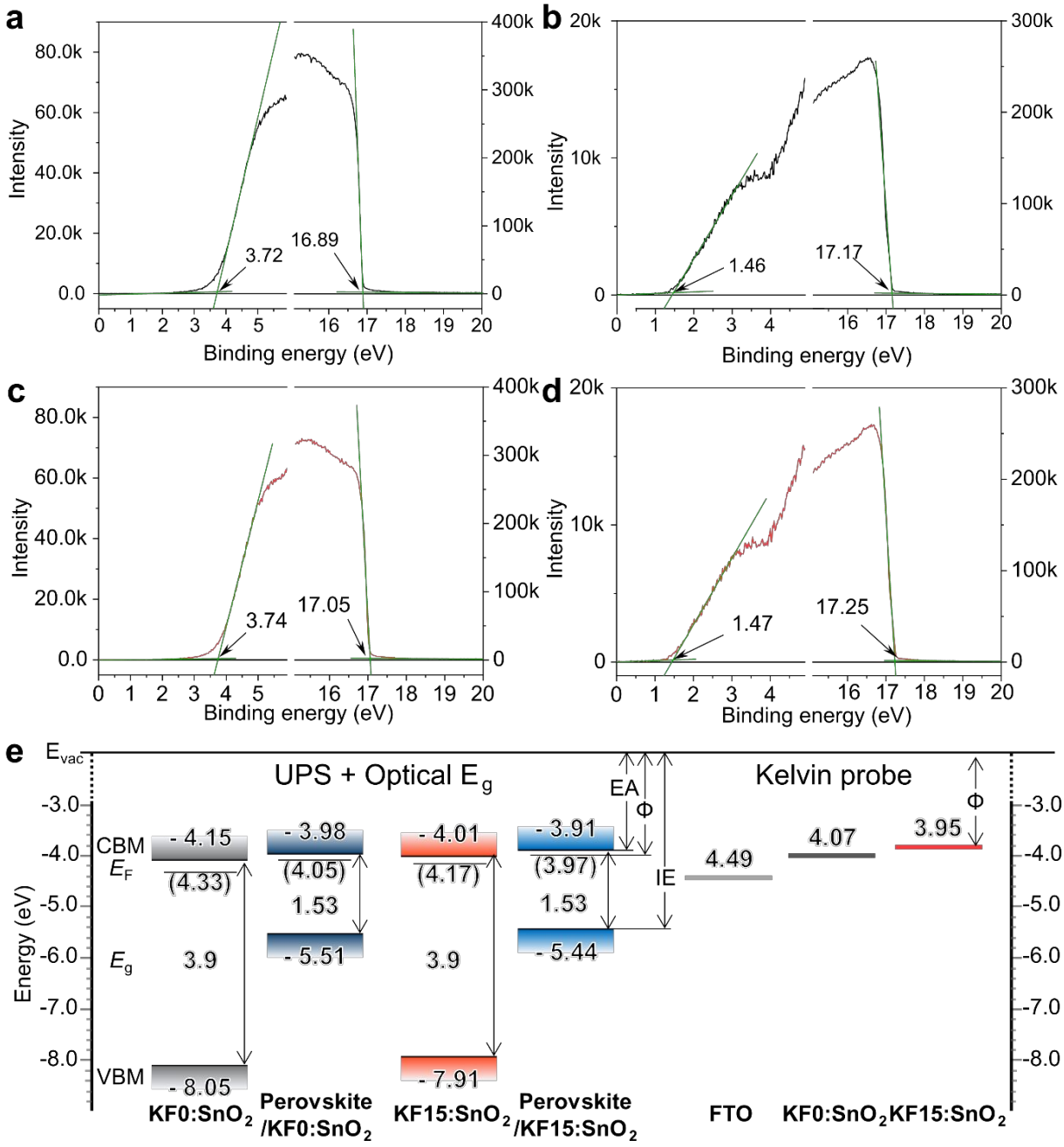

Figure 5. UPS spectra of the secondary electron cutoff region and valence band region for the (a) KF0:SnO_2, (b) perovskite on KF0:SnO_2, (c) KF15:SnO_2, and (d) perovskite on KF15:SnO_2. (e) Energy diagram with respect to the vacuum energy (E_{vac}), summarizing the energy level extracted UPS spectra, optical bandgap (E_g) (by UV–Vis spectroscopy, Figure S6), and contact potential difference by Kelvin probe (Figure S7). CBM, conduction band minimum; E_F, Fermi energy; VBM, valence band maximum; EA, electron affinity; IE, ionization energy; Φ, work function.

originated from the soda-lime glass,[46] the layer beneath FTO. Considering the potassium intensity in KF0:PSC is the baseline, KF15:PSC has a slightly higher detectable intensity of potassium than KF0:PSC, which suggests the remnant of potassium after device fabrication.

The electronic properties of the KF0:SnO_2 and KF15:SnO_2 were studied using ultraviolet photoelectron spectroscopy (UPS) and optical bandgap measurements. To understand the effect of KF additive in PSCs, the electronic structure of the perovskite layers deposited on both SnO_2 layers was also investigated, since the energy levels of the deposited perovskite can be influenced by the properties of the bottom substrate. Figures 5a–d present the valence band energy (E_{VB}) region (left) and secondary electron cutoff (E_{cutoff}) region (right) of the KF0:SnO_2, KF15:SnO_2, and subsequently deposited perovskite on the KF0:SnO_2 and KF15:SnO_2. The work functions (Φ) were derived by subtracting the E_{cutoff} from the standard He I irradiation energy to measure UPS (21.22 eV). The valence band maximum (VBM) was calculated by VBM=21.22 − (E_{cutoff} − E_{VB}), and the conduction band minimum (CBM) was determined using the VBM and optical bandgap (E_g). The E_g of each layer was determined by Tauc plot based on UV–Vis spectroscopy (Figure

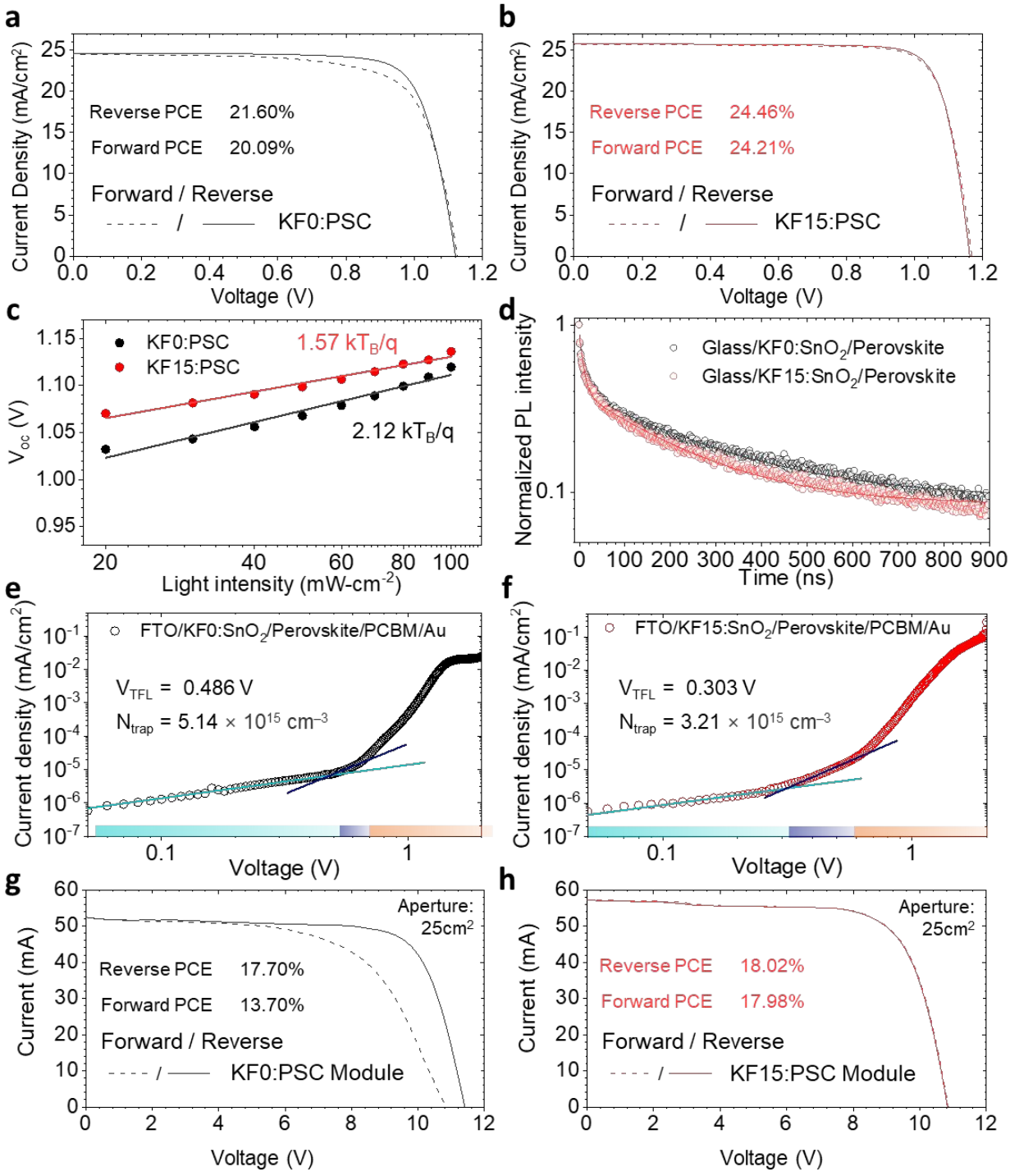

Figure 6. Current density–voltage *(J–V)* curve of the (a) KF0:PSC, and (b) KF15:PSC. (c) Light-intensity dependence of V_{oc} for KF0:PSC and KF15:PSC (d) Normalized time-resolved photoluminescence (TRPL) decay at 810 nm for the FTO/KF0:SnO_2/perovskite/P4VP and FTO/KF15:SnO_2/perovskite/P4VP. (e-f) Space charge limited current (SCLC) measurement of the electron only devices based on the FTO/KF0 and KF15:SnO_2/perovskite/PCBM/Au structure. *J–V* curve of the (g) KF0:PSC module, and (b) KF15:PSC module, fabricated with 25 cm^2 aperture area size.

S7). The E_F measured UPS was further validated through Kelvin probe force microscopy (KPFM), as shown in Figure S8. Although the exact values were not identical due to differences in the measurement environments and depths between UPS and KPFM, the E_F measured by both UPS and KPFM showed nearly similar values, and exhibited the same trend for both the KF0:SnO_2 and KF15:SnO_2. Figure 5e summarizes the energy structure of the SnO_2 and deposited perovskite, while Table S5 organizes the analyzed energy values. The results show that the overall energy level of the KF15:SnO_2 was about 0.14 eV higher than that of the KF0:SnO_2, while the CBM/E_F/VBM values of the KF15:SnO_2 were slightly higher than those of the KF0:SnO_2. These differences were attributed to the lower oxygen defect levels located below the CBM in the KF15:SnO_2,[47] as well as the

higher energy offset between the CBM of SnO_2 and VBM of perovskite, which could increase the V_{OC} of the PSC.[48] The lower energy offset between the CBM of SnO_2 and CBM of perovskite is beneficial for electron transport with reduced energy loss.[49] The optical properties of the samples were barely affected by the addition of the KF, with an optical E_g of around 3.89 eV for both SnO_2 layers, and 1.53 eV for both perovskite layers. Based on these findings, it is expected that the KF15:PSC will demonstrate better photovoltaic performance than the KF0:PSC.

Figures 6a and b present the current density–voltage (*J*–*V*) curve for the KF0:PSC and KF15:PSC, respectively, both with forward ($J_{SC} \rightarrow V_{OC}$) and reverse scan ($V_{OC} \rightarrow J_{SC}$) directions. The devices exhibited significant differences in performance, and Table S6 summarizes their photovoltaic factors. The KF15-based device demonstrates an average efficiency of 24.34 % with a negligible hysteresis index of 0.010, while the KF0 shows a reverse PCE of 21.60 % and a forward PCE of 20.09 %, with a hysteresis index of 0.075. We calculated the hysteresis index by dividing the PCE difference of scan direction by the PCE of the reverse scan. As can be observed in the cross-section and plane-view SEM images of the KF0:PSC and KF15:PSC (Figure S9), there were no discernible differences in the morphology or thickness of the perovskite layer formed on the SnO_2 samples, regardless of whether the KF was applied or not. This implies that the efficiency difference in the PSC depending on the application of KF is due to the favorable energy level of the KF15:SnO_2 and characteristics such as uniform coating, rather than morphological differences. Indeed, the results of the uniform coating were both an increase in PCE, and statistically more consistent results. As summarized in Figure S10, the statistical box chart of 50 independent devices shows that the KF15:PSC exhibits higher values for all photovoltaic parameters, while also forming a very narrow distribution. In contrast, the KF0:PSC shows very wide distribution, particularly in V_{OC} and FF, which is believed to be due to the influence of a non-uniform ETL. These statistical results can be confirmed by the standard deviation for each photovoltaic parameter. Furthermore, we measured the maximum power point (MPP) tracking capability of the champion device to evaluate the stabilized power generation (Figure S11). After being subjected to 1.5 AM simulated sunlight for 60 min in ambient air and applying the maximum power voltage, the device retained 90 % of its initial PCE, indicating that the high efficiency of the KF15:PSC is not overestimated.

These changes in performance of the PSCs based upon the addition of KF to SnO_2 are likely due to significant alterations in the charge carrier behavior, such as the transport or recombination of carriers generated in the perovskite layer. Therefore, various measurements related to optoelectronic charge carrier behavior were conducted to investigate such alteration in detail. In Figure 6c, the open-circuit voltage was measured under various light intensities ranging (1 to 0.1) Sun. In the diode equation, V_{OC} is given by

$$\frac{nkT}{q}\ln\left(\frac{I}{I_0}+1\right)$$

, where n is the ideality factor, k is the Boltzmann constant, T is the temperature, q is the charge of an electron, and I_o is the saturated dark current. The slope of V_{OC} *vs.* the logarithm of light intensity is determined by the n value. If the n value is close to 1, bimolecular recombination is the dominant process, whereas an n value close to 2 indicates trap-assisted recombination.[50] The KF0:PSC showed a higher n value of 2.12 than the KF15:PSC (n = 1.57), indicating that the KF additive can suppress trap-assisted recombination. The KF0:PSC even showed an ideality factor exceeding 2, implying the surface and interface recombination also occurred in addition to the trap-assisted recombination. It aligns with the analysis for the KF0:SnO_2 exhibiting poor passivation of the interface between SnO_2 and perovskite layers. Figure 6d shows the time-resolved photoluminescence (TRPL) measurement, and the spectra were fitted using a second exponential decay curve (see Table S7). The average lifetime of the KF15:PSC half device was 25 % lower than that of the KF0:PSC half device, suggesting that the KF-added SnO_2 improves the carrier transport efficiency between perovskite and ETL, and reduces carrier recombination.[51]

Figures 6e and f present the results of our space charge limited current (SCLC) measurements used to determine the trap density in the perovskite films. To do so, we prepared electron-only devices with the FTO/KF0:SnO_2 or KF15:SnO_2/Perovskite/PCBM/Au structure. We observed that the dark current increased linearly as all traps were filled by injected carriers. At the transition point, known as the trap-filled limit voltage (V_{TFL}), the current lost ohmic response, and the slope turned to over 3. By estimating V_{TFL}, we calculated the trap density (N_{trap}) using the equation $N_{trap} = (2\varepsilon\varepsilon_0 \cdot V_{TFL})/qL^2$, where ε is the dielectric constant, ε_0 is the vacuum permittivity, q is the charge of an electron, and L is the thickness of the film.[52] We used a literature value of ε = 46.9 and an L value of 700 nm from cross-sectional SEM images in Figure S9.[53] We found that the KF15:PSC-based electron-only device had a lower trap density (N_{trap} = 3.21 × 10^{15} cm^{-3}) than the KF0:PSC-based electron-only device (N_{trap} = 5.14 × 10^{15} cm^{-3}). Enhanced long-term stability for the KF15:PSC devices over KF0:PSC were confirmed by storing samples under the 60 ± 5% relative humidity condition for 250 hours (Figure S12). Significantly longer lifetime of KF15:PSC was mainly attributed to the superior charge carrier extraction efficiency and lower defect concentration of KF15:SnO_2 ETL.

Superior optoelectronic properties of KF15:SnO_2 verified by PSC devices and following characterization, along with the uniform distribution and deposition property of KF-treated SnO_2, contribute to enhancing the efficiency of large-area PSC modules. We thereby fabricated PSC modules with an aperture size of 5 × 5 cm^2 and 10 sub-cells using KF0:SnO_2 and KF15:SnO_2 as shown in Figures 6g and h. As a result, the KF0:PSC module exhibited a J_{SC} of 20.8 mA·cm^{-2}, V_{OC} of 11.40 V, FF of 74.46 %, and a PCE of 17.70 % in the reverse scan. However, in the forward scan, it showed a low performance of 13.70 % due to a sharp drop in V_{OC} and FF. Such severe hysteresis behavior is attributed to the non-uniform deposition of the SnO_2 ETL.

In contrast, the KF15:PSC module did not show hysteresis characteristics and achieved a J_{SC} of 22.9 mA·cm^{-2}, V_{OC} of 10.82

V, FF of 72.47 %, and a PCE of 18.02 % in the reverse scan. These results confirm that KF:SnO_2 not only has advantages in small-area devices but also in large-area modules, and suggest a method to improve widely used SnO_2-based ETLs through a simple processing.

Comparing the small device and module results, it is observed that the J_{SC} of the module is lower than that of the small device. It is mainly attributed that the small device is less affected by film uniformity, while in the module with an active area of 25 cm^2, film uniformity has a significant impact on J_{SC}. In this study, films were fabricated by spin-coating method to achieve high efficiency, allowing the analysis of the effect of KF-doped SnO_2. As a result, it is expected that the scaling-up and module fabrication processes contributed to the lower J_{SC} of module.

The KF15:PSC module still exhibited a higher J_{SC} than the KF0:PSC module, which is attributed to the superior uniformity of the SnO_2 ETL. The reduced hysteresis characteristics is also ascribed to the enhanced charge extraction by KF doping. If bar coating or blade coating processes that ensure perovskite film uniformity are adopted and laser process optimization is implemented for each ETL, it is expected that KF-doped SnO_2 ETL could achieve even higher efficiency in large-area devices.

Conclusions

This study presents a comprehensive investigation into the effects of potassium fluoride (KF) additives on the performance of the perovskite solar cell (PSC). We found that the addition of KF to the SnO_2 colloidal solution significantly improved the performance of the PSC, with an optimal concentration of 1.5 mg of KF in 1 mL of mixed solution. We attributed this improvement to several factors. Firstly, the addition of KF led to a reduction in aggregate size, which facilitated the formation of a more uniform film as an electron transport layer (ETL). Secondly, the change in zeta potential induced by KF addition improved the wettability of the SnO_2 colloidal solution on the FTO substrate, leading to a smoother and more conformal coating of SnO_2 nanoparticles. Thirdly, the presence of KF resulted in a more favorable energy level alignment between the SnO_2 ETL and the perovskite layer, which enhanced the photovoltaic performance of the PSC. Furthermore, the addition of KF to the SnO_2 colloidal solution did not significantly affect the dispersion stability, yet ensured wettability onto the FTO substrate. This led to a uniform coating in the fabrication process, which is crucial for the performance of the PSC. The KF15:PSC exhibited higher values for all photovoltaic parameters, while also forming a very narrow distribution, indicating more consistent results. Still, the proposed model with KF is based on a hypothesis and is supported by indirect results measured from the film and device. It is expected that the exact KF behavior can be proven through DFT-based computational approach, which could provide inspiration for the development of various additives in the future. In summary, our findings highlight the potential of KF additives to SnO_2-based ETL to enhance the performance of the PSC. This study provides valuable insights into the role of additives in colloidal solutions and their impact on the performance of the PSC, paving the way for the further optimization of the PSC for efficient solar energy conversion. Future work should focus on further optimizing the concentration of KF, and exploring other potential additives to improve the performance of the PSC.

Experimental

Materials

All the chemical regents are commercially available and used without further purification. All solvents, potassium fluoride (≥99.97% trace metals basis), 4-tert-butylpyridine, bis(trifluoromethylsulfonyl) imide lithium salt (Li-FTSI) were purchased from Sigma-Aldrich. Formamidinium iodide (FAI), formamidinium bromide (FABr), methylammonium iodide (MAI), methylammonium chloride (MACl), and [tris(2-(1H-pyrazol-1-yl)-4-tert-butylpyridine)-cobalt(III) tris(bis-(trifluoromethylsulfonyl)imide) (FK209) were purchased from GreatCell Solar. The SnO_2 Colloidal solution (SnO_2, 15wt% in H_2O) was obtained from Alfa Aesar. The hole transport material 2,2',7,7'-Tetrakis-9,9'-spirobifluorene (Spiro-OMeTAD), was purchased from Borun.

Solution preparation

Colloidal SnO_2 solution: SnO_2 dispersion solution was prepared by mixing purchased SnO_2 colloidal solution (0.2 mL) with the 0, 1.5, 3.0, 4.5, and 6.0 mg of KF dissolved high purity deionized H_2O (0.8 mL) by 1:4 volume ratio.

Perovskite precursor: The 1.5 M of PbI_2 dissolved in mixture of DMF and DMSO (9:1 volume ratio) and then stirred at 70 °C for overnight in N_2 glove box. For the mixed cation solution, 90 mg of FAI, 6.5 mg of MAI, and 9 mg of MACl mixed in 1ml isopropanol solution and stirred at room-temperature for 2 hours. For the champion device, we used 1.5 M of PbI_2 containing 1.5 mol% of cesium acetate. For the mixed halide solution 80 mg of FAI, 5mg of FABr, 6.5 mg of MAI, and 9 mg of MACl were dissolved in 1ml isopropanol.

Doped Spiro-MeOTAD solution: The solution of 70 mM spiro-MeOTAD in chlorobenzene was prepared with additives of Li-TFSI, FK209, tBP. The final molar ratio of additives for 0.53, 0.03, and 3.26 for Li-TFSI, FK209 and tBP, respectively.

Device fabrication

The glass/etched fluorine doped tin oxide (FTO)-glass substrates (TEC15, Pilkington) were cleaned sequentially using detergent, acetone, ethanol, and deionized water in an ultrasonic bath for 30 min, respectively. The prepared colloidal SnO_2 solution was spin coated onto glass/FTO substrate at 3000 rpm for 30 sec, and then annealed in ambient air at 150 °C for 30 min. the perovskite layer was deposited using sequential deposition method in N_2 glove box. Prepared PbI_2 solution was coated on SnO_2 layer at 1500 rpm for 20 sec and 5000 rpm for 30 sec. after PbI_2 had cooled down to RT, mixed cation halide solution was spin coated on the PbI_2 layer at 1800 rpm for 30 sec. After finish spin coating, the reddish-brown colored film was taken out to ambient air and annealed it at 140 °C for 25 min. After annealing, black phase perovskite film brought back to N_2 glove

box. The prepared Spiro-OMeTAD solution was coated at 4000 rpm for 30 sec using dynamic spin casting. Finally, 80 nm thick Au electrodes were deposited by thermal evaporation. The electrode area was 4 mm x 5 mm.

Modulization

Laser scribing was performed using a 532-nm picosecond laser (AOPico 532-5-1000, Advanced Optowave Corp) for perovskite module with 10 μm of beam diameter and 300 kHz of pulse repetition rate (PRR). Multiple lines (2, 10, and 10 lines each) were processed for P1, P2, and P3, respectively, with the 10 μm of line spacing. The laser power for P1 to separate FTO was optimized for 0.83 W with the 50 mm s^{-1} of scribing speed. The laser powers for P2 and P3 were 0.36 and 0.14 W, respectively with the 400 mm s^{-1} of scribing speed. The geometric fill factor (GFF) was 94.36% according to the total scribing widths from the summation of P1(25 μm), P2(120 μm), and P3(110 μm). Perovskite modules were fabricated with a designated area of 31cm^2, and an active area of 25 cm^2, and each module consisted of 10 sub-cells.

Characterization

Zeta potential and DLS were assessed using a Zetasizer nano series by Malvern Panalytical. The measurement of the contact angle was conducted using an Ossila setup, during which a video captured the perovskite solution dripping on the surface. A plane-view and cross-sectional SEM images were taken by using a Zeiss LEO1550. AFM was measured by PSIA XE150 with contact AFM. XPS were recorded using the instrument PHI Quantera II (Physical Electronics). Absorbance measurements of the perovskite layer were carried out using a UV-Vis spectroscopy system equipped with an Ocean Optics QE6500 spectrometer and a DH-2000-BAL light source. Photovoltaic properties were assessed using a Wave Labs SINUS-70 LED solar simulator equipped with UV and IR extenders. An automatic calibration system managed the light intensity, ranging from 10 to 100 mW cm^{-2}. *J–V* data were obtained at a scan rate of 100 mV s^{-1} using an Xtralien X200 (Ossila) source meter. A metal mask with a circular opening measuring 0.125 cm^2 defined the active area. Light intensity dependent V_{OC} and SCLC measurement was also conducted with the same setup. Time-resolved photoluminescence measurements were conducted using a Quantaurus-Tau C11367-12 fluorescence lifetime spectrometer from HAMAMATSU. A 464 nm laser (PLP-10, HAMAMATSU, with a peak power of 231 mW and a pulse duration of 53 ps, pulsing at a repetition rate of 2 MHz) served as the photoexcitation source. In the cyclic voltammetry experiment, the electrolyte consisted of 1 mM potassium ferricyanide and 1 mM potassium ferrocyanide dissolved in a 0.5 M potassium chloride aqueous solution as the supporting electrolyte. A platinum rod served as the reference electrode, while the working electrode was made from the SnO_2 film under investigation. The surface area of the samples was standardized by measuring a rectangular area of 1 by 1.2 cm. XRF (X-ray fluorescence) measurement was conducted at sector 2idd of the Advanced Photon Source at Argonne National Laboratory. A Fresnel zone plate focusing optics was used to produce a 14 keV monochromatic beam with 250-300 nm spot size. The sample was rasterized through the focused X-ray beam in a fly-scan mode with 200 ms exposure time per pixel and a step size of 300 nm. A full spectrum was collected at each pixel to construct 2D elemental maps. Per-pixel spectrum fitting was performed using MAPS software.[54]

Author contributions

B.J.K., M.-C.K., and G.B. conceived and designed the project. B.J.K., G.S., and S.P. fabricated the PSC devices. B.J.K., D.L. performed the material characterization, and Y.L. and S.W. performed synchrotron X-ray based material characterization. B.J.K., D.L. and M.-C.K. conducted the electrical analysis. B.J.K., M.-C.K. and G.B. wrote the original draft and all the authors reviewed and edited the paper.

Conflicts of interest

There are no conflicts to declare.

Data availability

The data supporting this article have been included as part of the ESI.

Acknowledgements

This work was supported by the National Research Foundation of Korea (NRF) grant funded by the Korean government (MSIT) (No. 2022R1C1C1003403). This work was also supported by the National Research Foundation of Korea Grant funded by the Korean Government (NRF-2020R1A6A3A03039130), the Swedish Energy Agency (43294-1) and the STandUP for Energy program. This work used resources of the Advanced Photon Source; a U.S. Department of Energy (DOE) Office of Science user facility operated for the DOE Office of Science by Argonne National Laboratory under Contract No. DE-AC02-06CH11357.

References

1 Sampaio, P. G. V. & González, M. O. A. Photovoltaic solar energy: Conceptual framework. Renewable and Sustainable Energy Reviews 74, 590-601 (2017).
2 Song, Z. et al. A technoeconomic analysis of perovskite solar module manufacturing with low-cost materials and techniques. Energy & Environmental Science 10, 1297-1305 (2017).
3 Li, J. et al. Perovskite single crystals: synthesis, optoelectronic properties, and application. Advanced Functional Materials 31, 2008684 (2021).
4 Lee, G. et al. Ultra-flexible perovskite solar cells with crumpling durability: Toward a wearable power source. Energy & Environmental Science 12, 3182-3191 (2019).
5 National Renewable Energy Laboratory, Best research-cell efficiency chart, accessed Feb 2024; https://www.nrel.gov/pv/cell-efficiency.html.

6 Wang, S. et al. Impacts of the hole transport layer deposition process on buried interfaces in perovskite solar cells. Cell Reports Physical Science 1 (2020).
7 Tavakoli, M. M., Yadav, P., Tavakoli, R. & Kong, J. Surface engineering of TiO2 ETL for highly efficient and hysteresis-less planar perovskite solar cell (21.4%) with enhanced open-circuit voltage and stability. Advanced Energy Materials 8, 1800794 (2018).
8 Jeon, J. B. et al. Photo-annealed amorphous titanium oxide for perovskite solar cells. Nanoscale 11, 19488-19496 (2019).
9 Cheng, M. et al. Charge-transport layer engineering in perovskite solar cells. Sci Bull 65, 1237-1241 (2020).
10 Wang, D., Wright, M., Elumalai, N. K. & Uddin, A. Stability of perovskite solar cells. Solar Energy Materials and Solar Cells 147, 255-275 (2016).
11 Kim, M.-c. et al. Degradation of CH 3 NH 3 PbI 3 perovskite materials by localized charges and its polarity dependency. Journal of Materials Chemistry A 7, 12075-12085 (2019).
12 Noh, M. F. M. et al. The architecture of the electron transport layer for a perovskite solar cell. Journal of Materials Chemistry C 6, 682-712 (2018).
13 Yang, G., Tao, H., Qin, P., Ke, W. & Fang, G. Recent progress in electron transport layers for efficient perovskite solar cells. Journal of Materials Chemistry A 4, 3970-3990 (2016).
14 Jiang, Q., Zhang, X. & You, J. SnO2: a wonderful electron transport layer for perovskite solar cells. Small 14, 1801154 (2018).
15 Park, S. Y. & Zhu, K. Advances in SnO2 for efficient and stable n–i–p perovskite solar cells. Advanced materials 34, 2110438 (2022).
16 Jiang, Q. et al. Surface passivation of perovskite film for efficient solar cells. Nature Photonics 13, 460-466 (2019).
17 Zhang, J. et al. Batch chemical bath deposition of large-area SnO2 film with mercaptosuccinic acid decoration for homogenized and efficient perovskite solar cells. Chemical Engineering Journal 425, 131444 (2021).
18 Guo, Y. et al. Vacuum thermal-evaporated SnO2 as uniform electron transport layer and novel management of perovskite intermediates for efficient and stable planar perovskite solar cells. Organic Electronics 65, 207-214 (2019).
19 Lee, Y. et al. Efficient planar perovskite solar cells using passivated tin oxide as an electron transport layer. Advanced Science 5, 1800130 (2018).
20 Huang, C. et al. Highly-Crystalline SnO2 Thin Films for Efficient Planar Perovskite Solar Cells. ACS Applied Energy Materials 5, 5704-5710 (2022).
21 Xu, Z., Zhou, X., Li, X. & Zhang, P. Polymer-Regulated SnO2 Composites Electron Transport Layer for High-Efficiency n–i–p Perovskite Solar Cells. Solar RRl 6, 2200092 (2022).
22 Liu, Z., Deng, K., Hu, J. & Li, L. Coagulated SnO2 colloids for high-performance planar perovskite solar cells with negligible hysteresis and improved stability. Angewandte Chemie 131, 11621-11628 (2019).
23 Bu, T. et al. Universal passivation strategy to slot-die printed SnO2 for hysteresis-free efficient flexible perovskite solar module. Nature communications 9, 4609 (2018).
24 Han, G. S. et al. Spin-coating process for 10 cm× 10 cm perovskite solar modules enabled by self-assembly of SnO2 nanocolloids. ACS Energy Letters 4, 1845-1851 (2019).
25 Najafpour, M. M. et al. Treated nanolayered Mn oxide by potassium fluoride: An improvement for nanolayered Mn oxide toward water oxidation. International Journal of Hydrogen Energy 41, 21203-21211 (2016).
26 Ramírez, O. et al. The effect of potassium fluoride postdeposition treatments on the optoelectronic properties of Cu (In, Ga) Se2 single crystals. Solar RRL 5, 2000727 (2021).
27 Gambinossi, F., Mylon, S. E. & Ferri, J. K. Aggregation kinetics and colloidal stability of functionalized nanoparticles. Advances in colloid and interface science 222, 332-349 (2015).
28 Zhu, J. H., Chun, Y., Qin, Y. & Xu, Q.-H. An investigation of KF modification to generate strong basic sites on NaY zeolite. Microporous and mesoporous materials 24, 19-28 (1998).
29 Keene, A. M. & Tyner, K. M. Analytical characterization of gold nanoparticle primary particles, aggregates, agglomerates, and agglomerated aggregates. Journal of Nanoparticle Research 13, 3465-3481 (2011).
30 Chappel, S. & Zaban, A. Nanoporous SnO2 electrodes for dye-sensitized solar cells: improved cell performance by the synthesis of 18 nm SnO2 colloids. Solar Energy Materials and Solar Cells 71, 141-152 (2002).
31 Gao, N. & Yan, Y. Characterisation of surface wettability based on nanoparticles. Nanoscale 4, 2202-2218 (2012).
32 Moore, T. L. et al. Nanoparticle colloidal stability in cell culture media and impact on cellular interactions. Chemical Society Reviews 44, 6287-6305 (2015).
33 Bhattacharjee, S. DLS and zeta potential–what they are and what they are not? Journal of controlled release 235, 337-351 (2016).
34 Shrestha, S., Wang, B. & Dutta, P. Nanoparticle processing: Understanding and controlling aggregation. Advances in colloid and interface science 279, 102162 (2020).
35 Xu, H. et al. Review of influence of steric effect on aggregation behavior of fine particles. Minerals Engineering 203, 108304 (2023).
36 Wen, T. & Majetich, S. A. Ultra-large-area self-assembled monolayers of nanoparticles. ACS nano 5, 8868-8876 (2011).
37 Santhanam, V., Liu, J., Agarwal, R. & Andres, R. P. Self-assembly of uniform monolayer arrays of nanoparticles. Langmuir 19, 7881-7887 (2003).
38 Luo, Y. et al. A Si-Substituted Spirobifluorene Hole-Transporting Material for Perovskite Solar Cells. ACS Energy Letters 8, 5003-5011 (2023).
39 Kwoka, M. et al. XPS study of the surface chemistry of L-CVD SnO2 thin films after oxidation. Thin solid films 490, 36-42 (2005).
40 Akgul, F. A. et al. Structural and electronic properties of SnO2. Journal of Alloys and Compounds 579, 50-56 (2013).
41 Lee, H. B. et al. Dopant-free, amorphous–crystalline heterophase SnO2 electron transport bilayer enables> 20% efficiency in triple-cation perovskite solar cells. Advanced Functional Materials 30, 2001559 (2020).
42 Wang, X. et al. Effect of oxygen vacancies on photoluminescence and electrical properties of (2 0 0) oriented fluorine-doped SnO2 films. Materials Science and Engineering: B 250, 114433 (2019).
43 Wang, H. et al. Hydrothermal synthesis of hierarchical SnO2 microspheres for gas sensing and lithium-ion batteries applications: Fluoride-mediated formation of solid and hollow structures. Journal of Materials Chemistry 22, 2140-2148 (2012). https://doi.org:10.1039/C1JM14839G
44 Garcia Romero, D. et al. Understanding the Surface Chemistry of SnO2 Nanoparticles for High Performance and Stable Organic Solar Cells. Advanced Functional Materials 34, 2307958 (2024).
45 Fang, F. et al. Mechanistic Understanding of Alkali-Metal-Ion Effect on Defect State in SrTiO3 During the Defect Engineering for Boosting Solar Water Splitting. Advanced Functional Materials 33, 2215242 (2023). https://doi.org:https://doi.org/10.1002/adfm.202215242
46 Rojas, L. et al. Lithographic fabrication of soda-lime glass based microfluidics. Nuclear Instruments and Methods in Physics Research Section B: Beam Interactions with Materials and Atoms 306, 296-298 (2013).

47 Sopiha, K. V., Malyi, O. I., Persson, C. & Wu, P. Chemistry of oxygen ionosorption on SnO2 surfaces. ACS Applied Materials & Interfaces 13, 33664-33676 (2021).
48 Baena, J. P. C. et al. Highly efficient planar perovskite solar cells through band alignment engineering. Energy & Environmental Science 8, 2928-2934 (2015).
49 Kim, B. J. et al. Interface design of hybrid electron extraction layer for relieving hysteresis and retarding charge recombination in perovskite solar cells. Advanced Materials Interfaces 5, 1800993 (2018).
50 Glowienka, D. & Galagan, Y. Light intensity analysis of photovoltaic parameters for perovskite solar cells. Advanced Materials 34, 2105920 (2022).
51 Wolff, C. M., Caprioglio, P., Stolterfoht, M. & Neher, D. Nonradiative recombination in perovskite solar cells: the role of interfaces. Advanced Materials 31, 1902762 (2019).
52 Chen, J., Kim, S.-G., Ren, X., Jung, H. S. & Park, N.-G. Effect of bidentate and tridentate additives on the photovoltaic performance and stability of perovskite solar cells. Journal of Materials Chemistry A 7, 4977-4987 (2019). https://doi.org:10.1039/C8TA11977E
53 Han, Q. et al. Single Crystal Formamidinium Lead Iodide (FAPbI3): Insight into the Structural, Optical, and Electrical Properties. Advanced Materials (Deerfield Beach, Fla.) 28, 2253-2258 (2016).
54 Vogt, S. in Journal de Physique IV (Proceedings). 635-638 (EDP sciences).

Data availability

The data supporting this article have been included as part of the ESI.